SUPPLEMENTARY INFORMATION
Measurement of Navier Slip on Individual Nanoparticles in Liquid

Jesse F. Collis,[†,‡] Selim Olcum,[†,§] Debadi Chakraborty,[‡] Scott R. Manalis[§,⊥,∥] and John E. Sader[*,‡]

[‡]ARC Centre of Excellence in Exciton Science, School of Mathematics and Statistics, The University of Melbourne, Victoria 3010, Australia
[§]Koch Institute for Integrative Cancer Research, Massachusetts Institute of Technology, Cambridge, MA 02139, USA
[⊥]Department of Biological Engineering, Massachusetts Institute of Technology, Cambridge, MA 02139, USA
[∥]Department of Mechanical Engineering, Massachusetts Institute of Technology, Cambridge, MA 02139, USA

[†]These authors contributed equally to the work.

*Email: jsader@unimelb.edu.au

CONTENTS

S1. MEASUREMENT SETUP

The suspended microchannel resonator (SMR) used in this study is a micro-cantilever with an integrated and embedded U-shaped microfluidtic channel; see Figures 1b and c. In contrast to conventional resonant mass sensors that are immersed in liquid, the SMR encapsulates the liquid environment inside the cantilever structure. The cantilever itself is contained in an on-chip vacuum chamber and vibrates in its resonant modes. This dramatically reduces viscous losses that would otherwise dominate the noise in mass measurements, thereby leading to extreme precision in frequency measurement. As a nanoparticle passes through the integrated channel, the cantilever's mass is transiently altered. This induces a brief, measurable change in the cantilever's resonant frequencies that is proportional to the buoyant mass of the particle. The frequency shift of the cantilever's third flexural mode is depicted in Figure 1c. Because higher-order eigenmodes of the cantilever each have a unique vibrational deflection function (mode shape),[1] the frequency shift signal acquired from each mode is different; see Figure 1d.

The core measurement technique used in this study relies on simultaneously exciting several higher-order eigenmodes of the SMR, while a single nanoparticle is flowed back-and-forth through the SMR. The vibration amplitudes are estimated to lie between 1nm and 40nm. Several checks are performed to ensure the overriding assumption of small amplitude and linear response is satisfied: (i) The amplitude of vibration is reduced until no cross-talk is observed between the different modes. (ii) The quality factors of the modes are measured at this low amplitude excitation and are independent of amplitude. (iii) The theoretical linear eigenmode shapes precisely match the experimentally measured mode shapes. (iv) At order amplitude squared, there is a flow at zero frequency and twice the driven frequency, due to the quadratic nonlinearity in the governing Navier-Stokes equations. These flow-induced frequencies are distinct from the SMR's (driven) modal frequencies and cannot contribute.

Slip at the particle surface affects each vibrational mode differently—due to their different excitation frequencies—and the effect of slip on these independent modes are measured concurrently.

To simultaneously acquire the frequency shift signals of multiple modes, the cantilever is configured as an oscillator with each mode having its own feedback loop; see Figure 1c and ref 1. Namely, the tip vibration of the SMR, which involves a superposition of all oscillated mode shapes, is measured using an optical lever setup. A custom circuit with adequate signal bandwidth (10 MHz) is utilized to condition, bandpass filter and amplify the signal acquired from a fast split-photodiode. To maintain linearity in the detected signal and prevent any crosstalk between different resonant modes, the gain of the photodetector is systematically reduced; this also prevents any signal saturation or clipping. The amplified detector signal is fed into a field programmable gate array (FPGA) through an analog-to-digital converter. The FPGA circuit is programmed to maintain an array of digital phase-locked-loops (PLL). Each PLL is dedicated to a single resonant mode and placed in closed-loop with the resonator, both to (i) demodulate the frequency variations of the vibrational mode, and (ii) excite the mode at a constant amplitude, as a particle induces a time-varying change in the cantilever at its resonant frequency. The theory of how a PLL should be configured to excite and de-modulate time-varying resonant frequency changes is discussed elsewhere.[1] In contrast to previous studies, this capability is extended up to the 6^{th} flexural mode of an SMR. During measurements, the loop bandwidth for each PLL controlling a specific mode is set to at least 250 Hz with a sampling rate of 1 kHz. Because each vibrational mode has a different frequency, the PLLs operate independently in the FPGA. Similarly, the actuation signals generated by each PLL are combined by the FPGA and amplified using an RF amplifier driving a piezo-ceramic actuator placed underneath the SMR chip. Multiple modes of the SMR are simultaneously and independently actuated by the ceramic actuator that concurrently vibrates at multiple frequencies; this is because each vibrational mode is responsive to signals only at its own resonant frequency.

To minimize the effects of uncertainty in the particle position and trajectory within the fluidic channel, frequency shifts of the first six resonant modes of the SMR (due to the passage of a single nanoparticle) are measured simultaneously. Fundamental mode 1 is not used in analysis because it does not contain nodes, which limits the ability to accurately determine particle position (Section S3). As a nanoparticle moves through the SMR, the measured frequency shift traces out the curves described by eq 2, i.e., the square of the mode shapes; see Figure 1d. This is used to extract the mass discrepancy parameter, α, for each mode, from which the nanoparticle radius and slip length are directly calculated (Section S3).

The requirement of wide and high channels (much larger than the particle size) and ability to control multiple modes simultaneously can increase the mass-equivalent noise in measurements relative to previously reported nanoparticle measurements.[2] To circumvent this problem, a microfluidic control method is used that was previously applied to monitor the buoyant mass of a single cell throughout its cell-cycle.[3] Specifically, the same nanoparticle is passed back and forth through the SMR's fluidic channel by controlling the fluidic pressures on both sides of the SMR. To enable this nanoparticle flow-control, long and separate fluidic channels (10 μm-wide and 625 μm-long) are connected to the SMR; see "Trap channels" in Figure 1b. After each individual particle measurement, the nanoparticle is held in these long channels for 2 seconds before being passed back into the SMR for the next single measurement.

Table S1. Dimensions of the SMR device used in this study.

Property	Dimension (μm)
SMR length	400
SMR width	19
SMR thickness	4
Channel height	3
Channel width	5
Lid thickness	0.5
Wall width	2

S2. DESIGN OF THE SUSPENDED MICROCHANNNEL RESONATOR

Behavior of the mass discrepancy parameter in the limit of small inertia, i.e., $\beta \ll 1$ (viscous dominated flow), is given asymptotically by $\alpha = 1 - (\sqrt{2}/9)(\gamma - 1)\beta^{3/2} + O(\beta^2)$ whereas in the opposite limit of high frequency, i.e., $\beta \gg 1$ (inviscid flow), we have $\alpha = 3/(1 + 2\gamma) + O(1/\sqrt{\beta})$; see eq 3 and Section S5 for the full derivation. This establishes that slip has no effect in these limits—slip affects the flow only at intermediate frequency, β. Therefore, it is important to use multiple vibrational modes of the SMR within this intermediate frequency range—enabling the optimal interrogation of slip. Moreover, to satisfy the underlying theoretical assumption of an unbounded flow, the dimensions (width and height) of the integrated fluidic channel must be much larger than the largest target particle diameter interrogated. To meet these criteria, an SMR with the dimensions and mechanical parameters reported in Table S1 is designed, fabricated and used. The SMR is fabricated in the Microsystems Technology Laboratories at MIT, with some steps performed at Innovative Micro Technology, Santa Barbara, CA, utilizing a previously described method.[4] The resonance properties of flexural modes 2 to 6 of the SMR are provided in Table S2. Fundamental flexural mode 1 (which is not used) has a resonant frequency of 34.796 kHz and quality factor of 20,761.

Table S2. Properties of flexural vibrational modes of the SMR detailed in Table S1.

Mode number	Unloaded frequency (MHz)	Quality factor	Standard deviation of frequency noise (Hz)
2	0.2180	9,440	0.43
3	0.6094	4,773	0.37
4	1.191	2,823	0.35
5	1.963	2,093	0.61
6	2.921	1,620	1.6

S3. OBSERVED BUOYANT PARTICLE MASS USING EACH SMR MODE

Experimental data for the frequency shift time series (e.g., see Figure 1d) is fit to eq 2 using an arbitrary polynomial (up to 3$^{\text{rd}}$ order) for the particle position, z_p, versus time, t, measurement. This fit procedure enables a nonlinear dependence of z_p on t to be accurately described—it is approximately linear. A least-squares method is applied to each mode and is used to simultaneously determine (i) the required mass ratio, $M_{\text{p}}^{\text{obs}}/M_{\text{SMR}}$, in eq 2, and (ii) the constants in the above-described (z_p vs t) polynomial function.

Calibration of SMR mass. To measure the observed buoyant mass of the particle, $M_{\text{p}}^{\text{obs}}$, the mass of the SMR, M_{SMR}, is required. This is determined using NIST-tracable polystyrene particles (ThermoFisher 4016A) of known mass. These particles have a well characterized radius of 793.5±9(SD) nm and a density of 1,050 kg/m^3. A total of 341 particles are measured using the SMR from a random sample of these NIST particles. The resulting measured radius of each particle is taken as the average of two measurements: the particle travels through each arm of the SMR's microfluidic channel as it traverses from one "buried channel" to the other (on the other side of the SMR); see Figure 1c. The temperature is monitored to be between 22.4 to 23.0°C throughout the calibration procedure. Because these polystyrene particles are much lighter than the gold particles used in the slip measurements, their motion relative to the SMR's solid walls is small. As such the effects of slip are minimal; this is evident from eq 4 in the limit, $\gamma \to 1$.

Equations 2–4 with $b = 0$ (no-slip) are used to analyze the 341 observed mass measurements of the NIST particles, producing a histogram of the normalized particle mass, $M_{\text{p}}^{\text{obs}}/M_{\text{SMR}}$. The SMR's mass, M_{SMR}, is then chosen such

that the mean of this histogram matches the mean of the NIST specified particle mass. This results in an SMR mass of $M_{\mathrm{SMR}} = 5.387 \pm 0.026 \times 10^{-11}$ kg, where the reported 95% C.I. is the combination of (i) the uncertainty specified by two standard errors of the measured mean particle radii, and (ii) the uncertainty due to temperature variation. This value for M_{SMR} is used in all gold nanoparticle measurements that interrogate slip.

To explore sensitivity to the (no-slip) assumption of $b = 0$ used in these calibration measurements, the same procedure is applied with $b = 10$ nm and $b = 100$ nm where the SMR mass is determined to be 5.386×10^{-11} kg and 5.377×10^{-11} kg, respectively—a change in SMR mass of only 0.02% and 0.2%, respectively, which is smaller than the reported uncertainty in M_{SMR} above. This shows that the hydrodynamic flow generated by these particles, and associated boundary condition at the polystyrene-water interface, exert a negligible effect on the measured SMR mass and can be safely ignored.

Gold nanoparticle measurements. Details of the gold nanoparticles used in measurements are in Section S4. For each of the five measured SMR modes (modes 2 to 6, see Figure 2b), the observed buoyant mass of each gold nanoparticle is determined using eq 2. Typical frequency changes due to the presence of a nanoparticle are approximately 1 to 10 Hz and always greater than the standard deviation of the frequency noise (which enables detection of the required signal). Equation 3 then gives the value of $\alpha M_{\mathrm{p}}^{\mathrm{true}}$, where the true buoyant mass of the particle is $M_{\mathrm{p}}^{\mathrm{true}} = (4\pi/3)R^3(\rho_{\mathrm{p}} - \rho_{\mathrm{f}})$; ρ_{p} is the known particle density, i.e., density of gold, and ρ_{f} is the known liquid density, i.e., density of water at the measured temperature (between 22.4 and 23.4°C for the gold nanoparticle measurements). The mass discrepancy parameter, α, is a function of the unknown particle radius, R, and slip length, b; see eq 4. A nonlinear least-squares approach is used with eq 4 to extract the two required parameters, R and b, from the (five independently measured) mass versus frequency data of the same particle (one measured mass for each vibrational mode, i.e., SMR modes 2 to 6). For the present experiments, slip lengths of a few nanometers will alter the measured frequency shift curves by approximately 0.01–0.1 Hz, relative to the no-slip result. Because these changes in the frequency shifts due to slip are expected to be much smaller than the standard deviation of the frequency noise (on the order of 1Hz, see Table S2), each nanoparticle measurement is repeated hundreds of times; see Table S3. Cumulative histograms of the radius and slip length for an individual nanoparticle are then generated; see Figure 3a for an example of these distributions.

Table S3. Measured radius, slip length and number of measurements on each gold nanoparticle. Reported uncertainty is two standard errors of the mean.

Radius (nm)	Slip length (nm)	Number of measurements
119.8±0.4	2.6±2.4	144
122.8±0.4	4.5±2.7	140
125.2±0.4	3.4±2.2	204
125.6±0.4	3.1±2.1	162
128.5±0.3	2.1±1.6	308
131.4±0.4	2.5±1.8	110
131.9±0.6	3.3±2.7	142
135.3±0.5	3.0±2.2	132
143.4±0.5	0.2±1.7	120
148.3±0.4	3.7±1.6	334
151.5±0.4	3.9±1.8	396
153.2±0.3	4.1±1.4	612
153.5±0.4	1.8±1.7	186
154.9±0.3	1.6±1.3	490
155.7±0.4	3.5±1.6	238
160.5±0.4	3.7±2.1	254
160.8±0.4	1.3±1.3	338

S4. SELECTING APPROPRIATE GOLD NANOPARTICLES

Stabilized suspensions of gold nanoparticles in citrate buffer from Sigma-Aldrich (742066, 742074, 742082 and 742090) are used for all slip measurements. These nanoparticles have identical composition and surface chemistry, but vary in size. The developed theory in Section S5 assumes a rigid, spherical particle of constant density. However, the true composition of these particles features a citrate layer, of thickness (<1 nm), adsorbed to the particle surface.[5] Because these layers are of low density, soft and compliant, they must produce an even smaller negative bias in the

measured slip length, i.e., they cannot account for the measured positive slip length reported in Figure 4. These citrate layers do modify the wettability of the gold surface, which affects the slip length; this property is used to compare the measured slip length to molecular simulations. The nanoparticles are sampled from populations with mean radii ranging from 100 to 200 nm.

To ensure only a single gold nanoparticle is in the channel at any given time, we use the following procedure. First, a low particle concentration of 10^4 to 10^5 particles per ml is supplied to the SMR channel. Second, we use the frequency versus time curves acquired from the multimode measurements (e.g., see Figure 1d) to test for the presence of more than one particle. If two particles are in the SMR simultaneously, a convolution of two different signals is measured; this looks drastically different to a single particle signal; e.g., see Figure 4 of ref 1. Occasional measurements of this type are discarded.

A total of 22 gold nanoparticles are measured (hundreds of times each, see above) whose radii vary from 67.9 to 205.0 nm. Slip lengths of a subset of these particles are interrogated, for the following reasons. Reducing the particle size lowers the signal-to-noise ratio, restricting the practical minimum radius that can be measured to 115 nm; see Figures 4a and 8. Conversely, the derived theory implicitly assumes the particle does not interact hydrodynamically with the bounding solid walls of the SMR, leading to a practical upper limit on the particle radius of 165 nm (above which, leads to errors in the measured slip length of greater than 1 nm); see Section S7. The full data set (including those particles not analysed as discussed above) is given in Figure S4a.

17 individual nanoparticles lie within this particle size range allowed by the measurement setup: radii between 115 and 165 nm. Use of these particles thus permits a robust assessment of the constitutive nature of the Navier slip condition. An analysis of the various uncertainties is provided next; error bars derived from this analysis are included in the data reported.

Sources of uncertainty. There are three key sources of uncertainty in the particle measurements: (i) a finite number of particle measurements leads to inevitable uncertainty in the measured means of the histograms, (ii) the temperature is measured to vary between 22.4 and 23.4°C (for the gold nanoparticle measurements) which alters the density and viscosity of the liquid, and (iii) measurement of the cantilever mass has uncertainty detailed in Section S3. All these uncertainties can be quantified and are independent, so the total uncertainty is the RMS of these values; the reported uncertainties in Table S3 give two standard errors of the mean.

S5. THEORETICAL MODEL FOR THE MASS DISCREPANCY PARAMETER

Functional dependence of the mass discrepancy parameter, α, on the liquid and particle properties, and the excitation frequency, f_n, is calculated under the following assumptions: (i) the particle is a solid sphere, (ii) its radius, R, is much smaller than the SMR length, L, and (iii) the particle oscillation amplitude is small relative to R. In addition, analytical calculations also assume that the particle is much smaller than the channel height and width, and far from any of the internal walls, i.e., the flow is unconfined. These assumptions enable linearization of the Navier-Stokes equations for the liquid surrounding the particle, and solution of the mass discrepancy parameter, α, at any local position, z_p, along the SMR.

We consider a spherical particle oscillating with velocity, $V\mathrm{e}^{-i\omega t}\hat{\mathbf{z}}$ (where V is to be determined), in a uniform oscillatory flow, $U\mathrm{e}^{-i\omega t}\hat{\mathbf{z}}$, where ω is the angular oscillation frequency, t is time, i is the imaginary unit, $\hat{\mathbf{z}}$ is the Cartesian unit vector in the direction of the oscillatory flow and the true velocities (as measured) are given by the real or imaginary part of these expressions. Because the flow exhibits negligible amplitude relative to the particle radius, R, we use the unsteady Stokes equations,

$$-i\beta\mathbf{u} = -\nabla p + \nabla^2\mathbf{u}, \tag{S1}$$

in the frequency domain with an explicit time dependence of $\mathrm{e}^{-i\omega t}$, where the variables in eq S1 have been nondimensionalized as follows: velocity by U, time by $1/\omega$, spatial dimensions by R, and the pressure scale is chosen for convenience to be $\mu U/R$ where μ is the shear viscosity of the fluid, $\beta = \omega R^2\rho_\mathrm{f}/\mu$ is the oscillatory Reynolds number and ρ_f is the fluid density. All variables in this section are henceforth dimensionless.

Using a reference frame where the far field velocity is zero introduces a fictitious force, $-(4\pi/3)i\beta\hat{\mathbf{z}}$, on the particle. The boundary conditions on the particle surface are therefore

$$\begin{aligned}\left[\mathbf{u}^{(d)} - (V-1)\,\hat{\mathbf{z}}\right]\cdot\mathbf{n} &= 0,\\ \left[\mathbf{u}^{(d)} - (V-1)\,\hat{\mathbf{z}} - \lambda\,\mathbf{n}\cdot\mathbf{S}\right]\cdot(\mathbf{I}-\mathbf{nn}) &= \mathbf{0},\end{aligned} \tag{S2}$$

where $\mathbf{n}$ is the unit normal to the particle surface, $\mathbf{I}$ is the identity tensor, $\lambda \equiv b/R$ is the Navier slip length (nondimensionalized by the particle radius) and $\mathbf{S} \equiv 2\mathbf{e} = \nabla\mathbf{u} + (\nabla\mathbf{u})^T$ where $\mathbf{e}$ is the rate-of-strain tensor. Solving

for the force on the particle gives $\mathbf{F} = -(4\pi/3)i\beta\hat{\mathbf{z}} + F^{(d)}\hat{\mathbf{z}}$, where

$$F^{(d)} = -6\pi\,(V-1)\,\frac{1+(1-i)\sqrt{\frac{\beta}{2}} - i\frac{\beta}{9} + \lambda\left(2+(1-i)\sqrt{2\beta} - i\beta/3 - \frac{(1+i)\beta}{9}\sqrt{\frac{\beta}{2}}\right)}{1+\lambda\left(3+(1-i)\sqrt{\frac{\beta}{2}}\right)}. \tag{S3}$$

Setting $\lambda = 0$ yields the well known result for (no-slip) Stokes drag on an oscillating sphere. The particle velocity, V, is specified by conservation of momentum,

$$-\frac{4\pi}{3}i\beta\gamma V = -\frac{4\pi}{3}i\beta + F^{(d)}, \tag{S4}$$

where $\gamma \equiv \rho_{\mathrm{p}}/\rho_{\mathrm{f}}$ is the ratio of the particle density to that of the liquid. The change in force on the SMR due to the presence of the particle is then calculated by subtracting the contribution from the bulk fluid in the absence of the particle and then integrating the remainder of the surface stress (now due only due to the disturbance flow created by the particle) over the surface of the SMR's microfluidic channel. This is achieved by using a bounding surface (whose shape is arbitrary) that is infinitely far away from the particle. The result of this procedure subsequently gives the observed buoyant mass of the particle. Dividing this by the true buoyant mass of the particle gives the required result for the mass discrepancy parameter in eq 4.

We now examine the effect of the liquid-solid particle boundary condition and first consider particles that impose the no-slip condition. For particles heavier than the surrounding liquid, $\gamma > 1$, (negative) buoyancy effects cause the particle to move relative to the liquid. Specifically, while inertia causes the particle to lag behind the solid motion of the SMR, hydrodynamic drag works to move the particle in concert. Since inertia inevitably wins as frequency increases, this leads to a reduction in the observed buoyant particle mass relative to its true value, i.e., α decreases as observed in the solid green and red curves of Figure 2a. This explains the measurements in Figure 3c of ref 1, as recently reported in ref 6. Particles lighter than the liquid lead to positive buoyancy, and hence an enhancement in the observed mass, i.e., the mass discrepancy parameter, α, exceeds unity (solid blue curve Figure 2a). Yan *et al.*[6] solved this "no-slip" problem numerically using a Lattice Boltzmann method, and the formula in eq 4 provides the analytical counterpart.

Slip at the solid surface reduces hydrodynamic drag and thus enhances deviation of the mass discrepancy parameter, α, from unity. A monotonic increase in the magnitude of this deviation in α with dimensionless slip-length, λ, is observed within the bounds for λ reported in Figure 2a. This deviation enables the slip length to be extracted from SMR measurements of nanoparticle mass.

S6. EFFECT OF PARTICLE NONSPHERICITY ON SLIP LENGTH MEASUREMENTS

Due to their synthesis process, gold nanoparticles are not perfectly spherical—but the measurement protocol is insensitive to nonsphericity, which we show here. The nanoparticles assume a random orientation in the SMR and hundreds of measurements are taken on each nanoparticle. Therefore, it is appropriate to study the ensemble average effect of nonsphericity over all possible particle orientations. In Section S6.1, we prove that this averaging procedure—inherent in our measurements—extracts the radius of an equivalent volume sphere to $O(\xi)$, where ξ is the RMS surface roughness, defined below.

Numerical simulations of nonspherical particles, using finite element analysis, shows that there exists a bias to the slip length at $O(\xi^2)$. See Section S6.2 for the complete numerical analysis; a general theory for this $O(\xi^2)$ effect will be reported elsewhere. These numerical simulations are used to quantify the influence of nonsphericity on the measured slip length—nonsphericity of the nanoparticles is characterized using transmission electron microscopy (TEM). Critically, this produces a *negative* slip length bias and is one order-of-magnitude smaller than the positive slip lengths reported here (bias is -0.18 ± 0.03 nm; 95% C.I.); it therefore cannot account for the measurements. Note that this bias is often termed an "effective slip length" in the literature.[7]

S6.1. Theoretical model for the effect of nonsphericity

Following the work of ref 8, the nonspherical particle is a superposition of a shape perturbation function, g, and the surface of a perfect sphere; the $O(1)$ function, g, is dimensionless. The radial coordinate of the particle surface is therefore,

$$r = 1 + \xi g(\theta, \phi), \tag{S5}$$

where r has been nondimensionalized by the radius of an equivalent volume sphere, θ and ϕ are the usual spherical polar and azimuthal angles, respectively and ξ is the RMS of the difference in the radial coordinates of the particle's surface and the surface of an equivalent volume sphere; identical scalings to Section S5 are used for all remaining variables. The no-slip boundary condition is applied to the particle surface throughout this section, however, the conclusions hold equally for particles with small slip lengths relative to their radii, by linearity, and are hence directly applicable to this study. The shape perturbation function, g, is normalized by

$$\frac{1}{4\pi}\int_{\hat{S}} g^2 dS = 1, \tag{S6}$$

where $\hat{S}$ is the surface of the unit sphere; this ensures that ξ specifies the RMS surface roughness as discussed above.

We now prove that the observed slip lengths obtained assuming a perfect sphere, i.e., eq 2–4, are unaffected by nonsphericity to $O(\xi)$. The force on the nonspherical particle for any fixed orientation is[8]

$$\mathbf{F} = \left[F_0\mathbf{I} + \xi\mathbf{A}^{(1)}\right]\cdot\mathbf{U}, \tag{S7}$$

where $\mathbf{U}$ is the (arbitrary) velocity of the particle and

$$F_0 = -6\pi\left(1 + (1-i)\sqrt{\frac{\beta}{2}} - i\frac{\beta}{9}\right), \tag{S8}$$

is the force coefficient of an equivalent volume sphere. The tensor representing the first order surface perturbation is

$$\mathbf{A}^{(1)} = \frac{9}{4}\left(1 + (1-i)\sqrt{2\beta} - i\beta\right)\int_{\hat{S}} g\,\mathbf{nn}\,dS. \tag{S9}$$

We now prove that $\mathrm{tr}(\mathbf{A}^{(1)}) = 0$, where tr denotes the trace of the tensor. Now

$$\mathrm{tr}(\mathbf{A}^{(1)}) = \frac{9}{4}\left(1 + (1-i)\sqrt{2\beta} - i\beta\right)\int_{\hat{S}} g\ \mathrm{tr}(\mathbf{nn})\,dS, \tag{S10}$$

but $\mathrm{tr}(\mathbf{nn}) = 1$ and $\int_{\hat{S}} g\,dS = 0$,[8] so we immediately have

$$\mathrm{tr}(\mathbf{A}^{(1)}) = 0. \tag{S11}$$

To calculate the mass discrepancy parameter, α, at arbitrary fixed particle orientation, the z-component of the force exerted on the particle when it moves with velocity $\mathbf{U} = (V-1)\hat{\mathbf{z}}$ is required, i.e.,

$$\mathbf{F}\cdot\hat{\mathbf{z}} \equiv F^{(d)} = (V-1)\hat{\mathbf{z}}\cdot\left[F_0\mathbf{I} + \xi\mathbf{A}^{(1)}\right]\cdot\hat{\mathbf{z}}, \tag{S12}$$

which gives

$$F^{(d)} = (V-1)\left[F_0 + \xi\boldsymbol{A}^{(1)} : (\boldsymbol{zz})\right], \tag{S13}$$

where **:** is the tensor double contraction operator. Note that the fictitious force due to the noninertial reference frame, as discussed in Section S5, must be included when calculating the mass discrepancy parameter, α. The ensemble average over all orientations then immediately follows from eqs S11 and S13,

$$\left\langle F^{(d)}\right\rangle \equiv \frac{1}{4\pi}\int_{\hat{S}} F^{(d)} dS = (V-1)\left(F_0 + \frac{\xi}{3}\,\mathrm{tr}(\mathbf{A}^{(1)})\right) = (V-1)F_0. \tag{S14}$$

This proves that eq 4, which assumes a perfect sphere, recovers the true slip length correct to $O(\xi)$. In so doing, it establishes that the effect of nonsphericity on the average hydrodynamic force, $\left\langle F^{(d)}\right\rangle$, must occur at higher order, and is therefore expected to be $O(\xi^2)$; see Section S6.2.

S6.2. Bias in the Measured Slip Length due to Particle Nonsphericity

Numerical simulations are performed on prolate spheroids and a regular dodecahedron. (i) Prolate spheroids are chosen because this geometry defines the lowest-order spherical harmonic for nonsphericity. Their results thus provide the leading-order effect for an arbitrary particle of small nonsphericity, and hence a good approximation. (ii) A regular dodecahedron is chosen because it mimics the faceted shape of the particles used in experiments; see Figure S1. Analysis of this particle validates the expected leading-order behavior of the prolate spheroid. The spherical theory in eq 4 is fit to these numerical results to estimate the magnitude of the bias in the slip length induced by nonsphericity. As discussed above, the no-slip boundary condition is used throughout.

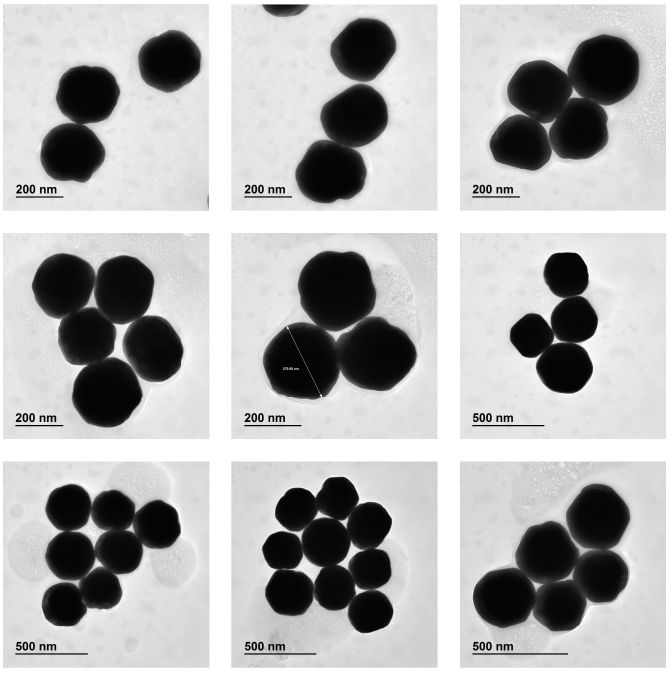

Figure S1. Transmission electron microscope images of Au nanoparticles. The nonspherical parameter, ξ, and equivalent radius, a_{equiv}, to be used in eq S15, are estimated from these images.

A. Prolate spheroids

Three prolate spheroids with major-to-minor axes ratios of 1.1, 1.3 and 1.5 (simply referred to as the "aspect ratio") and a sphere are studied. The force on each particle due to unitary translation along each principal axis is calculated at the 5 frequencies used in the experiments; see Table S2. This is achieved via numerical computation using COMSOL Multiphysics. That is, the counterpart of eq S3 for a nonspherical particle is computed. Due to linearity of the unsteady Stokes equations, the force in 3 orthogonal directions is sufficient to calculate the force in any (random) orientation. The numerical value of the mass discrepancy parameter, α, is calculated from these computational results.

Monte-Carlo simulations are then performed as described in Section S8 but, importantly, the prolate spheroidal particle assumes a random orientation for each run, the results of which are averaged; the order of this averaging process is irrelevant for small ξ. These simulations show that for prolate spheroidal particles, SMR measurements recover the radius of the equivalent volume sphere correct to $O(\xi)$, as expected; see Figure S2. Indeed, the numerical results suggest that this holds to $O(\xi^2)$; see caption of Figure S2. This shows that use of the equivalent volume sphere surface as the reference surface in the reported slip length measurements is appropriate.

The mean slip length extracted from Monte-Carlo simulations of each prolate spheroid, using the spherical formula in eq 4, is plotted in Figure S3a. Because the above theory shows there is no bias in the slip length to $O(\xi)$, a quadratic term in ξ is fit to the simulation results; this yields

$$b_{\text{bias}}^{\text{prol}} = -(0.65 \pm 0.23)\xi^2 a_{\text{equiv}}, \tag{S15}$$

where $b_{\text{bias}}^{\text{prol}}$ is the (dimensional) slip length bias and a_{equiv} is the radius of the equivalent volume sphere; a 95% C.I. is specified. It is noteworthy that the slip length bias, b_{bias}, is always negative and the fit parameter of 0.65 ± 0.23 is of order one, as expected from dimensional considerations. Since a prolate spheroid defines the lowest-order spherical harmonic for nonsphericity, as discussed, the result in eq S15 is expected to provide a good approximation for an arbitrary particle of small nonsphericity.

B. Regular dodecahedron

The above numerical analysis is repeated for a regular dodecahedron, i.e., the force on the particle when vibrating in each of 3 orthogonal directions is calculated numerically with COMSOL at each of the 5 experimental frequencies. The

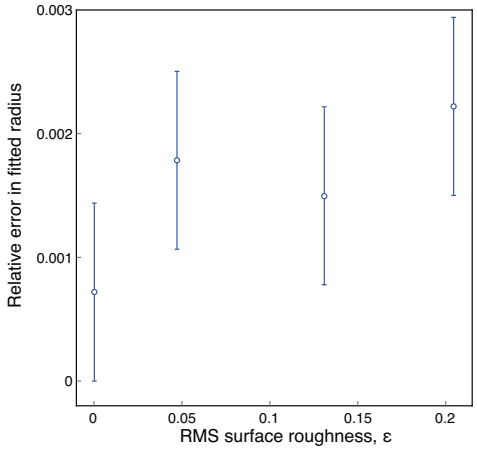

Figure S2. Error in the equivalent spherical radius extracted from numerical simulations of prolate spheroids. The relative error is RE $\equiv (a_{\rm equiv} - a_{\rm sim})/a_{\rm equiv}$, where $a_{\rm equiv}$ is the radius of an equivalent volume sphere and $a_{\rm sim}$ is the radius extracted by fitting numerical simulations to eq 4. Because $\xi = 0$ defines a sphere, RE is due to (i) numerical simulation error, and (ii) bias due to nonsphericity. Since the radius extracted using the spherical model, eq 4, is correct to $O(\xi)$—see Section S6.1—it follows that the extracted radius is expected to vary quadratically with ξ (at next order). A quadratic fit with respect to ξ gives RE $= (0.06 \pm 0.04)\xi^2$, where the uncertainty specifying two standard errors. This shows there is no bias in the measured equivalent radius to $O(\xi^2)$; the fit coefficient is small and its error is comparable to its value.

dodecahedron studied has an equivalent volume sphere radius of 150nm. These numerical results are used to calculate the mass discrepancy parameter from which the above-mentioned Monte-Carlo simulations are used to determine the bias in the slip length. Due to the theoretical arguments in Section S6.1, we expect this slip bias to be $O(\xi^2)$. For the dodecahedron shape we calculate $\xi = 0.058$ and extract a slip length of -0.44 ± 0.08nm. Dividing by the particle's equivalent volume sphere radius, and ξ^2, i.e., the expected order of the error, gives

$$b_{\rm bias}^{\rm facet} = -(0.86 \pm 0.16)\xi^2 a_{\rm equiv}. \tag{S16}$$

The bias is again of the order $\xi^2 a_{\rm equiv}$ as indicated by the order one constant in eq S16. This result is virtually identical to eq S15 for a prolate spheroid, highlighting (i) the leading-order nature of the prolate spheroid result, and (ii) validity of the asymptotic analysis for both smooth and faceted particles (the experimental situation). The formula for a prolate spheroid is used to estimate the slip length bias in all measurements.

Reference 7 shows that for a no-slip, rough, and flat surface in steady Stokes flow, there is an effective slip length—defined at the location of the mean roughness height—which is always negative and varies as $O(\xi^2)$. The above negative slip length biases, $b_{\rm bias}^{\rm prol}$ and $b_{\rm bias}^{\rm facet}$, for nonflat (spherical) surfaces in unsteady Stokes flow exhibit the same sign, magnitude and dependence on ξ as ref 7.

TEM images are used to measure the values of ξ and $a_{\rm equiv}$ for the nanoparticles studied; see Figure S1. MATLAB is used to numerically integrate the particle shape contour and thus calculate both the equivalent radius, $a_{\rm equiv}$, and nonspherical parameter, ξ. These values are substituted into eq S15 to estimate the bias, $b_{\rm bias}$, in the observed slip length of each particle, the results of which are given in Figure S3b. The mean value of this slip length bias over all measured particles is $\langle b_{\rm bias} \rangle = -0.18 \pm 0.03$ nm (95% C.I.) which is well within the uncertainty of the observed slip length in the experiments of $b = 2.7 \pm 0.6$ nm (95% C.I.). This bias due to nonsphericity has an insignificant effect on the final measured slip lengths and their uncertainties in Figure 4.

S7. EFFECT OF THE SMR WALLS ON SLIP LENGTH MEASUREMENTS

The disturbance velocity field created by the particle (when inside the SMR) is inviscid outside the particle's viscous boundary layer. In this outer region, it decays as $1/r^3$ where r is the radial distance from the particle center. For the present experiments, the viscous boundary layer thickness is between 200 and 800 nm, which is smaller than the channel width and height. This rapid decay in the disturbance flow minimizes the effect of the SMR walls on the measurements.

To quantify wall effects on the slip measurements, numerical simulations are performed for finite channel size. A boundary integral method (described in Section S11) is used. Simulations are performed on no-slip particles to create

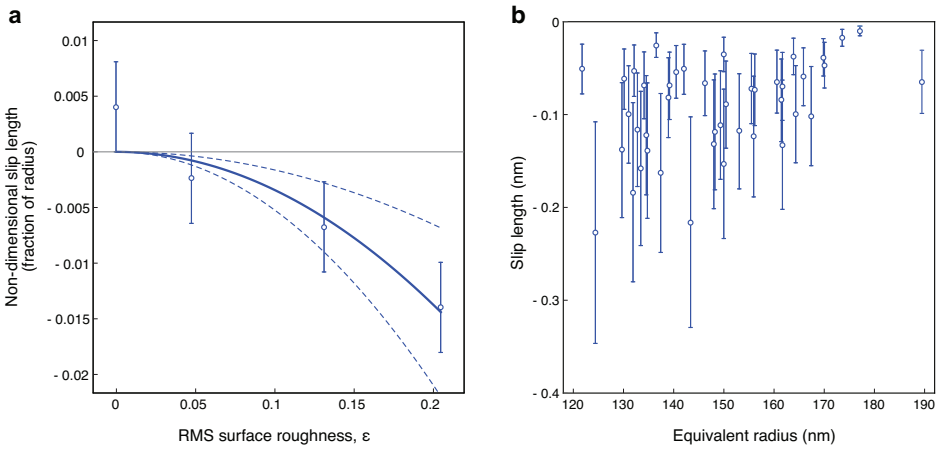

Figure S3. Bias in the slip length measurements due to nonsphericity. (a), Bias in the observed slip length for prolate spheroidal particles. Note that $\xi = 0$ corresponds to a sphere and hence the evident deviation from zero at this value specifies the uncertainty in the numerical computations. The solid curve gives the quadratic best fit to the data set (i.e., slip length is chosen to vary as ξ^2) and the dashed curves specify its corresponding 95% C.I. The resulting fit equation is given in eq S15. (b), Corresponding slip length bias, b_{bias}, estimated using eq S15 for each particle in Figure S1; error bars specify a 95% C.I. based on the error in the numerical computations (from panel a).

sample data of $\alpha M_{\text{p}}^{\text{true}}$ vs β. The same procedure used for the experiments as described in Section S3 is then used to extract the radius and slip length from this sample data. If the SMR walls exert no effect, then the extracted slip length will be zero and the extracted radius will be equal to the specified (true) particle radius. Numerical results show that these two properties always occur simultaneously allowing for slip length evaluation to be used as a proxy for wall effects. While these simulations of wall bias use the no-slip boundary condition, they apply equally to particles with slip by linearity (provided the slip length is much smaller than the particle radius, which is the experimental situation).

Transit times (which vary between 300 and 800 ms for each half of the SMR) are used to estimate the particle's proximity to the SMR walls (fast transit times indicate particle paths close to the center of the microfluidic channel while slow transit times imply paths closer to the bounding walls). Laminar flow through a pipe of rectangular cross section is used for this purpose; the effect of the particle on this flow is ignored due to its small size. Because there is variability in the flow rate through the SMR, calculation of the precise position of the particle within the SMR is not possible; this error is included in the error bars of Figure S4 (95% C.I.). In general, particles close to the SMR walls have a large negative bias to the slip length while particles far from any walls do not experience any bias. Figure S5 gives (sample) results for a 150 nm radius particle in a 3 μm height channel, as a function of particle position in the channel. This shows that a significant (negative) slip length bias occurs only if the particle is placed a distance less than 25% of the channel height from the wall. From the measured transit times, we conclude that the vast majority of particles do not lie close to the internal walls—the remaining particles (close to the walls) exert a negligible effect on the overall slip measurements. The primary finding of our numerical simulations is that particles of radius smaller than 160 nm induce a negligibly small bias in slip (due to the walls) while particles of radius close to 200 nm experience a detectable negative bias in the extracted slip length. Therefore, these larger particles are excluded from the final analysis; see Figure S4 for the full data set, including these excluded particles. Importatntly, the experimental nonideality of the boundary walls produces negative slip length biases only, its presence cannot explain the measured positive slip lengths in Figure 4.

S8. MONTE CARLO SIMULATIONS

The overall performance of the described methodology for measuring the true radius and slip length of a single particle is assessed here using Monte Carlo simulations. Simulations are performed where synthetic frequency shift data are generated using eq 2, for a chosen (nominal) particle mass, radius, density ratio and slip length. Gaussian frequency noise with the same standard deviation found in the measurements of each SMR mode (see the fourth column in Table S2) is added to this synthetic frequency shift data; this produces simulated data resembling the curves in Figure 1d. The particle radius and slip length are then recovered from this noisy synthetic data using an identical procedure to that of the measurements, i.e., a least squares procedure is used with eqs 2–4 to determine R

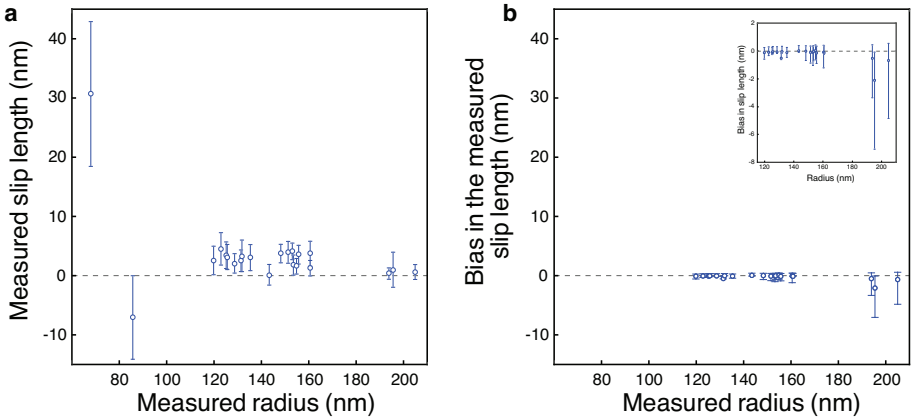

Figure S4. Bias in extracted slip length measurements resulting from a wall-bounded flow. (a), Measured slip length and 95% C.I. for the 22 particles studied. The smallest two particles (radii 67.9 and 85.7 nm) are excluded from the data analysis for unacceptable signal-to-noise ratio; see Figure S9. (b), Bias in the measured slip length due to finite size effects within the SMR (vertical bars specify a 95% C.I.). The largest 3 particles (radii 193.9, 195.8 and 205.0 nm) exhibit a significant negative bias in their measured slip length due to the bounding wall. Numerical simulations are not performed on the 2 smallest particles that are eliminated for unacceptable signal-to-noise ratio. Identical vertical scales are used in panels a and b to facilitate comparison, with details of panel b magnified in its inset.

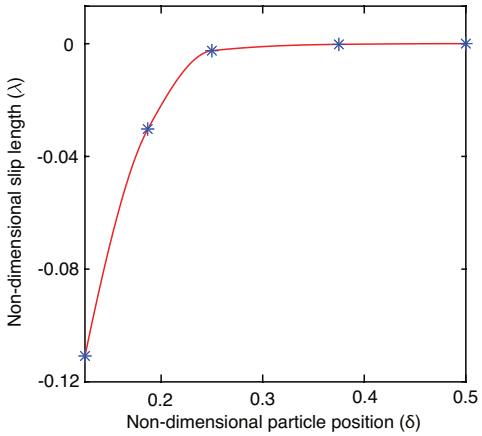

Figure S5. Effect of bounding wall on the extracted slip length. Sample numerical (boundary element) simulations of a 150 nm radius gold nanoparticle with a no-slip boundary condition in a finite sized channel of height 3 μm (identical to the SMR used). A nondimensional slip length, $\lambda \equiv b/a$, where b is the slip length and a is the particle radius, is fitted using the small particle analytical fornula, eq 4. A fitted slip length of zero indicates that the assumptions underlying eq 4 are satisfied, i.e., the particle is hydrodynamically isolated from the channel walls. The nondimensional particle position is $\delta \equiv z/a$, where z is the distance between the channel's lower wall and the particle center. Blue stars are the boundary element simulations, red line is to guide the eye. Numerical uncertainty in the boundary integral calculations are comparable to the starred symbols.

and b from modes 2 to 6 (see Section S3 for a detailed description).

In total, 10,000 simulations are performed using this procedure on a single particle specification, resulting in histograms for both the extracted particle radius and slip length. Initially, a particle radius and slip length of 125 nm and 5 nm, respectively, is studied to test the efficacy of the data fitting procedure. The resulting radius and slip length histograms for these simulations are provided in Figure 3b. The histogram for the radius appears to be normally distributed with a mean of 125.03±0.06 nm, i.e., the particle radius of 125 nm is extracted accurately. Additionally, the variance of this histogram matches the experimental data, demonstrating that frequency noise is the direct cause of the variance in the experimental particle radius distributions. In contrast, the slip length histogram is right skewed, as in the experimental data. The variance and the skewness coefficient match the experimental data, again indicating the shape of these distributions is a direct consequence of frequency noise. The mean of the slip length distribution is 6.91±0.24 nm which exceeds the specified slip length of 5 nm; this discrepancy is now discussed.

To explore the difference between the specified and extracted mean slip lengths, as a function of frequency noise,

we run a set of Monte Carlo simulations where the frequency noise is systematically increased from zero (all other details are as described above). This is achieved by fixing the relative strengths of the frequency noise standard deviations across all vibrational modes to the experimental situation, and increasing their magnitudes; Figure 3c reports the results of these simulations. Because the mass discrepancy parameter, α, is proportional to the frequency shift of each mode, Δf_n (see eqs 2 and 3), adding noise to the frequency shift curves is equivalent to adding noise directly to the mass discrepancy parameter, α. We therefore report the average standard deviation of the mass discrepancy parameters over all modes on the horizontal axis in Figure 3c. The mean slip length (extracted from the slip length distributions) appears to increase quadratically with increasing noise, suggesting the actual slip length can be determined if the noise level is known.

An asymptotic analysis—in the limit of small frequency noise—is now performed on the least-squares fit procedure used to determine R and b. That is, the primary (leading-order) effect of skewness in the histograms is considered. This gives a formula connecting (i) the *measured mean slip length and particle radius* of each data set and (ii) the frequency noise of each SMR vibration mode, to the *actual slip length and particle radius* corresponding to the Navier slip condition. We provide the full derivation of this procedure (Section S8.1) and then subsequenctly validate its usage through Monte Carlo simulations (Section S8.2). Importantly, by performing a large number of measurements on an individual particle, the noise can be well characterized allowing for the recovery of the actual slip length.

S8.1. Asymptotic theory for least-squares fits in the presence of additive noise

This analysis builds on the theory reported in ref 9. Dimensional variables are used predominantly in this section. The least-squares procedure for the multimode measurements fits a specified number, N, of observed buoyant mass measurements, $M_p^{(k)}$, to a known fit function, $F(\mathbf{X}, \beta_k) = \alpha M_p^{\text{true}}$, where $\mathbf{X} \equiv (R, b)$, β_k is the oscillatory Reynolds number of mode k, and M_p^{true} is the true buoyant mass. The required fit is obtained by adjusting the parameters, $\mathbf{X}$, such that the function,

$$\Delta = \sum_{k=1}^{N} \left[F(\mathbf{X}, \beta_k) - M_{\text{p}}^{(k)} \right]^2, \tag{S17}$$

is minimized. Here, we theoretically examine the performance of this least squares procedure in the presence of an additive noise process in the collected data, specifically $M_{\text{p}}^{(k)} = \hat{M}_{\text{p}}^{(k)} + \epsilon z_k$ where $\hat{M}_{\text{p}}^{(k)}$ is the (idealized) measurement in a noiseless system; ϵz_k models the noise process where the constant $\epsilon \ll 1$ and $\{z_k\}$ is a set of independent $O(1)$ random variables. Therefore, the variance of the measurement is $\text{Var}[M_{\text{p}}^{(k)}] = \epsilon^2 \text{Var}[z_k]$. Here, ϵ^2 is chosen to be the mean of the variances of all measured modes, i.e., $\epsilon^2 = \text{E}(\text{Var}[M_{\text{p}}^{(k)}])$ with $\text{E}(\text{Var}[z_k]) = 1$. The least squares fit procedure in eq S17 therefore becomes

$$\Delta = \sum_{k=1}^{N} \left[F(\mathbf{X}, \beta_k) - \hat{M}_{\text{p}}^{(k)} - \epsilon z_k \right]^2. \tag{S18}$$

Stationary points of the system are specified when the gradient of Δ with respect to $\mathbf{X}$ is zero, i.e., $\partial_{\mathbf{X}} \Delta = \mathbf{0}$, giving

$$\sum_{k=1}^{N} \left(F(\mathbf{X}, \beta_k) - \hat{M}_{\text{p}}^{(k)} - \epsilon z_k \right) \partial_{\mathbf{X}} F(\mathbf{X}, \beta_k) = \mathbf{0}, \tag{S19}$$

which specifies a set of simultaneous equations equal to the number of dimensions of $\mathbf{X}$; which is two in the present problem. We define an asymptotic expansion for $\mathbf{X}$ with respect to ϵ,

$$\mathbf{X} = \mathbf{X}_0 + \epsilon \mathbf{X}_1 + \epsilon^2 \mathbf{X}_2 + O\left(\epsilon^3\right), \tag{S20}$$

where $\mathbf{X}_0$ is the fit parameter vector in the limit of zero noise, i.e., the (required) true value of the fitting parameters. A Taylor expansion of the fit function about $\mathbf{X}_0$ gives

$$F(\mathbf{X}, \beta_k) = F_k + \epsilon \mathbf{X}_1 \cdot \partial_{\mathbf{X}} F_k + \epsilon^2 \left(\mathbf{X}_2 \cdot \partial_{\mathbf{X}} F_k + \frac{1}{2} \mathbf{X}_1 \cdot \partial_{\mathbf{X}}^2 F_k \cdot \mathbf{X}_1 \right) + O\left(\epsilon^3\right), \tag{S21}$$

where F_k and its derivatives are the corresponding values of F evaluated at $(\mathbf{X}_0, \beta_k)$. Taylor expansion in the gradient about $\mathbf{X}_0$ gives

$$\partial_{\mathbf{X}} F(\mathbf{X}, \beta_k) = \partial_{\mathbf{X}} F_k + \epsilon \mathbf{X}_1 \cdot \partial_{\mathbf{X}}^2 F_k + O\left(\epsilon^2\right). \tag{S22}$$

Substituting eqs S21 and S22 into eq S19 and collecting terms of $O(1)$ leads to

$$\sum_{k=1}^{N} \left(F_k - \hat{M}_{\mathrm{p}}^{(k)} \right) \partial_{\mathbf{X}} F_k = \mathbf{0}, \tag{S23}$$

whose solution, $\mathbf{X}_0$, is the required result in the absence of noise.

Next, equating the terms of $O(\epsilon)$ in eq S19 and solving for $\mathbf{X}_1$ gives,

$$\mathbf{X}_1 = \sum_{k=1}^{N} z_k \mathbf{b}_k, \tag{S24}$$

where

$$\mathbf{b}_k = \mathbf{A}^{-1} \cdot \partial_{\mathbf{X}} F_k \qquad \text{and} \qquad \mathbf{A} = \sum_{k=1}^{N} \partial_{\mathbf{X}} F_k \; \partial_{\mathbf{X}} F_k. \tag{S25}$$

The expected value and variance of the first order correction, $\mathbf{X}_1$, are therefore

$$\mathrm{E}[\mathbf{X}_1] = \sum_{k=1}^{N} \mathrm{E}[z_k] \, \mathbf{b}_k, \tag{S26}$$

$$\mathrm{Var}[\mathbf{X}_1]_{[m]} = \sum_{k=1}^{N} \mathrm{Var}[z_k] \, [\mathbf{b}_k]_{[m]}^2 \,, \tag{S27}$$

where $[m]$ denotes the m^{th} component of the vector. The expected value of the noise is zero in practice, i.e., $\mathrm{E}[z_k] = 0$. Therefore, eq S26 shows that the expected value of the first order correction to the required solution is also zero, i.e., $\mathrm{E}[\mathbf{X}_1] = \mathbf{0}$. Thus, to $O(\epsilon)$ the least squares procedure extracts the required parameters accurately in measurement.

Collecting the $O\big(\epsilon^2\big)$ terms and solving for $\mathbf{X}_2$ gives

$$\begin{aligned} \mathbf{X}_2 = \mathbf{A}^{-1} \cdot \sum_{k=1}^{N} \Bigg(& z_k \mathbf{X}_1 \cdot \partial_{\mathbf{X}}^2 F_k \\ & - \frac{1}{2} \left(\mathbf{X}_1 \cdot \partial_{\mathbf{X}}^2 F_k \cdot \mathbf{X}_1 \right) \partial_{\mathbf{X}} F_k - \left(\mathbf{X}_1 \cdot \partial_{\mathbf{X}} F_k \right) \mathbf{X}_1 \cdot \partial_{\mathbf{X}}^2 F_k \Bigg). \end{aligned} \tag{S28}$$

Unlike the $O(\epsilon)$ correction in eq S26, the expected value of $\mathbf{X}_2$ is generally not zero when the expected value of the noise, $\mathrm{E}[z_k]$, is zero. This has an important consequence to estimation of the true parameters: *there will be bias in the parameter estimate from the least squares procedure.* This bias is calculated using eqs S24 and S28 to be

$$\begin{aligned} \mathrm{E}[\mathbf{X}_2] = \mathbf{A}^{-1} \cdot \sum_{k=1}^{N} \Bigg(& \mathrm{E}\big[z_k^2\big] \, \mathbf{b}_k \cdot \partial_{\mathbf{X}}^2 F_k \\ & - \sum_{j=1}^{N} \mathrm{E}\big[z_j^2\big] \left(\frac{1}{2} \left(\mathbf{b}_j \cdot \partial_{\mathbf{X}}^2 F_k \cdot \mathbf{b}_j \right) \partial_{\mathbf{X}} F_k + \left(\mathbf{b}_j \cdot \partial_{\mathbf{X}} F_k \right) \mathbf{b}_j \cdot \partial_{\mathbf{X}}^2 F_k \right) \Bigg), \end{aligned} \tag{S29}$$

where F_k and its derivatives are specified at $\mathbf{X}_0$; see eq S21. Thus, eq S29 defines the second order correction to the fit parameters in the presence of noise in terms of the required (noiseless) fit parameters, $\mathbf{X}_0$.

It is observed in eq S29 that if the curvature of the fitting function is nonzero, i.e., the tensor $\partial_{\mathbf{X}}^2 F_k$ is nonzero, there will be a nonzero bias due to the presence of noise. The true value of the required parameters, $\mathbf{X}_0$, is calculated by solving

$$\mathrm{E}[\mathbf{X}] = \mathbf{X}_0 + \epsilon \, \mathrm{E}[\mathbf{X}_1] + \epsilon^2 \, \mathrm{E}[\mathbf{X}_2] + O\big(\epsilon^3\big) \,, \tag{S30}$$

where $\mathrm{E}[\mathbf{X}_1] = 0$ in practice, as discussed above.

Figure S6 shows the utility of eq S30 by comparison to Monte Carlo simulations (10,000 individual simulations per data point) where excellent agreement is observed; see Section S8.2 for details.

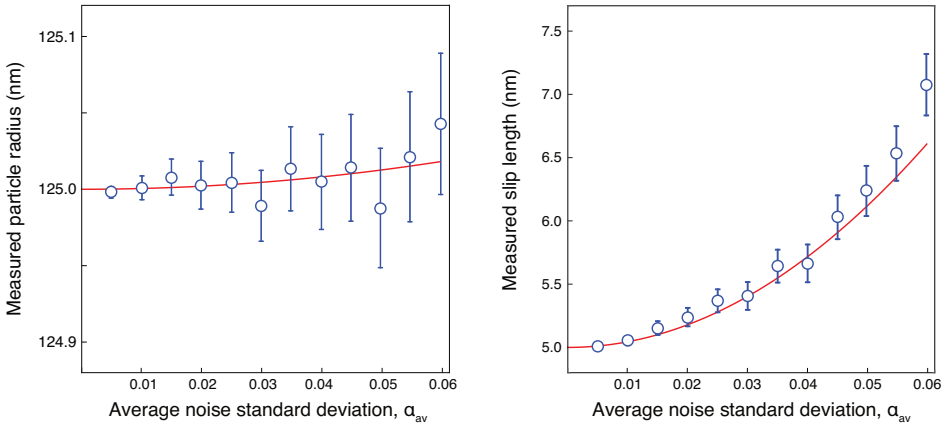

Figure S6. Effect of noise on the extracted fit parameters using the least squares procedure. Monte Carlo simulations showing bias in the mean radius and slip length extracted using the least squares procedure, for the described SMR system with a hypothetical 125 nm radius gold particle with a 5 nm slip length. Data for the measured slip length is identical to Figure 3c. The horizontal axis specifies the average standard deviation of the mass discrepancy parameter, α_{av}, which coincides with that of the relative frequency noise over all modes; $\alpha_{\mathrm{av}} = 0.0401$ is the experimental value from the measurements. Red curves are theoretical results from the derived asymptotic theory, eq S30. Blue dots are the mean of Monte Carlo simulations with 10,000 runs; error bars specify 2 standard errors of the mean. Equation S30 accurately predicts the observed bias of the fitting procedure in the Monte Carlo simulations.

S8.2. Monte-Carlo simulations of the methodology to measure particle radius and slip length

The overall performance of the described methodology for measuring the true radius and slip length of a single particle is further assessed here using Monte Carlo simulations with details of the implementation as discussed previously. This extends simulation data presented in Figure S6 by examining performance as the slip length and particle radius are varied systematically. Simulations are performed by generating theoretical frequency shift curves for vibrational modes 2 to 6 from eqs 2–4, for a specified radius and slip length; reported on the axes/captions of Figures S7 and S8. A fixed frequency noise level of $\epsilon \equiv \alpha_{\mathrm{av}} = 0.0401$ corresponding to the experimental value (from Table S2) is used throughout this section; ϵ is defined in Section S8.1.

Varying the slip length: A 150 nm radius spherical particle is used whose specified slip length is systematically varied—10,000 individual simulations are performed for each radius/slip length combination. Output of the Monte Carlo simulations is analyzed using the least squares procedure detailed in Section S8.1; eq S30 is used to remove bias induced by the added noise. Results of this analysis are given in Figure S7 which shows that the described procedure accurately extracts the particle radius and slip length within 2 standard errors of the mean.

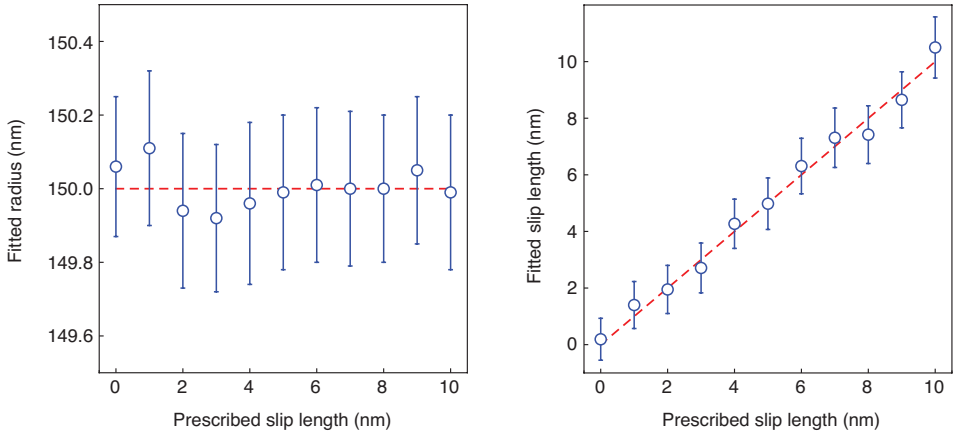

Figure S7. Monte Carlo simulations of least squares procedure to extract the true radius and slip length. Monte-Carlo results for 150 nm gold particles using the noise level from experimental while systematically varying the slip length. 10,000 simulated particle measurements are used for each slip length. The radius and slip length are subsequently fitted in the same manner as the experimental measurements. Red dashed lines are the specified (and expected) result and blue dots are the mean results of the Monte-Carlo simulations with errors bars for 2 standard errors of the mean. The radius and slip length are accurately determined in all cases.

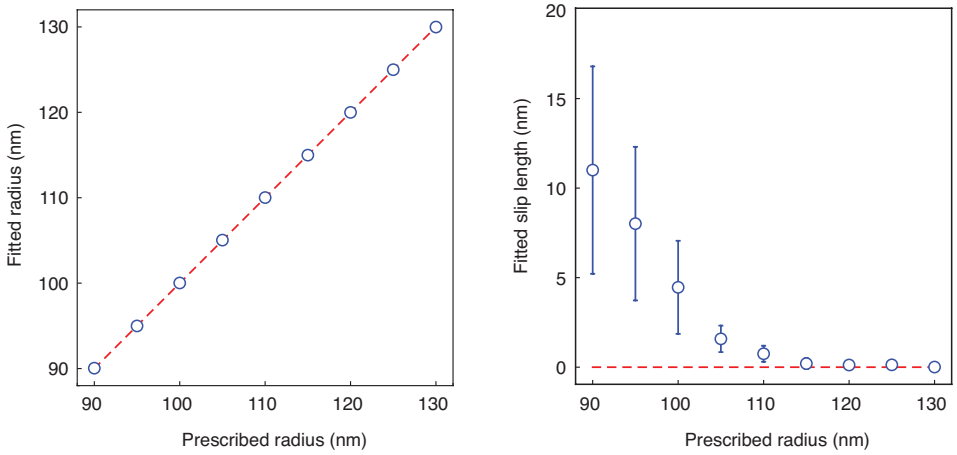

Figure S8. Effect of noise on the least squares procedure for extracting the true radius and slip length—no-slip particle. Monte-Carlo results for no-slip particles using the noise level from experiment while varying the particle radius. 10,000 simulated particle measurements are used for each specified radius, from which the radius and slip-length are extracted using the least squares procedure. For particles of radii greater than ∼115 nm the analysis correctly recovers the expected no-slip result (red dashed line). Blue dots are means of the Monte-Carlo simulations with errors bars specifying 2 standard errors of the mean.

Varying the particle radius: In contrast, Figure S8 shows results where no-slip is specified at the particle surface and the particle radius is varied. The radius and slip-length are then extracted from Monte Carlo simulation data using the same least squares procedure. Because the relative frequency shift, $\Delta f_n/f_n$, increases linearly with the observed buoyant particle mass, the relative added noise is inversely proportional to this mass (i.e., the radius cubed) in Figure S8. Consequently, the asymptotic theory in eq S30 is expected to break down for small particle size where the noise becomes relatively large (violating a primary constraint of the asymptotic theory). Indeed, it is observed that for particles of radius smaller than ∼115 nm, the extracted slip length is inaccurate. This data also shows that the use of small particles leads to small signal-to-noise (large error bars) which limits the ability to accurately measure the slip length; see Figure S9 for examples of the frequency measurements for particles with different radii.

S9. STATISTICAL ANALYSIS OF SLIP LENGTH VERSUS RADIUS DATA

A statistical analysis using linear regression is performed to test for independence of the slip length on particle radius. A high p-value ($p = 0.57$) is observed indicating there is no evidence for a correlation between radius and measured slip length. Moreover, the R^2 value of this linear regression is very small 0.018 ($\ll 1$). Hypothetically, if the p-value were to be small (e.g., less than 0.05), this minute R^2 value would indicate that the radius accounts for 2% of the observed variance in the measured slip length—which is also negligible. Thus, regardless of the p-value there is no statistically significant and meaningful relationship between the measured slip length and particle radius. A similar conclusion arises if a higher-order polynomial is used.

S10. MEASURED FREQUENCY SHIFT CURVES VERSUS PARTICLE SIZE

Figure S9 shows sample measured data for the frequency shifts of modes 2 to 6 of the SMR used in this study. Increasing the particle size clearly increases the measured signal-to-noise ratio, facilitating measurement. This data is complementary to that presented in Figure 1c; Figure S9b is identical to Figure 1c.

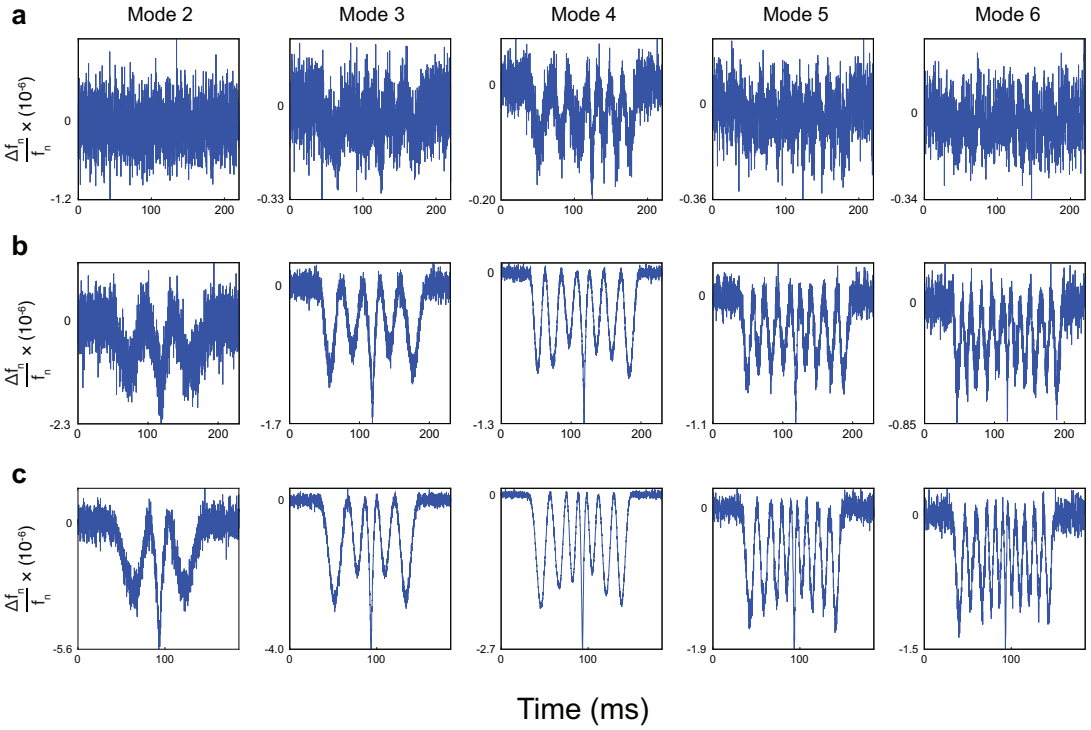

Figure S9. Measured relative frequency shifts for modes 2 to 6 of the SMR. Sample frequency shift signals of gold nanoparticles as they pass through the SMR's microfluidic channel. Particles with radii (a), 67.9 nm, (b), 125.6 nm and (c), 205.0 nm. The two larger particles have a large signal-to-noise ratio allowing for a robust fit of the radius and slip length. The larger particle in panel c, however, is affected by the bounding wall and thus the fitted slip length is inaccurate (see Figure S4b)—it is not used in the final reported measurements. The signal-to-noise ratio of the smallest particle shown is low which hinders accurate measurement of its slip length.

S11. A BOUNDARY INTEGRAL METHOD FOR WALL-BOUNDED FLOWS

The numerical procedure for the results presented in Section S7 is now detailed. Nondimensional variables are used throughout with identical scalings to Section S5. A boundary element method is used to numerically solve the flow specified by the unsteady Stokes equations, eq S1. The boundary integral equation for the velocity field, $\mathbf{u}$, at a point,

$\mathbf{r}_0$, on the surface S of a domain is

$$\begin{aligned}\mathbf{u}(\mathbf{r}_0) = &-\frac{1}{4\pi}\int_S \mathbf{f}(\mathbf{r})\cdot\mathbf{G}(\mathbf{r}-\mathbf{r}_0)\,dS(\mathbf{r}) \\ &+\frac{1}{4\pi}PV\int_S \mathbf{u}(\mathbf{r})\cdot[\mathbf{T}(\mathbf{r}-\mathbf{r}_0)\cdot\mathbf{n}(\mathbf{r})]\,dS(\mathbf{r})\,,\end{aligned} \tag{S31}$$

where $\mathbf{r}$ and $\mathbf{r}_0$ are position vectors from the origin. We choose $S \equiv S_p \cup S_c$ with S_p to be the particle surface and S_c the bounding (internal) walls of the SMR, $\mathbf{f}(\mathbf{r})$ is the distribution of surface forces, $\mathbf{G}(\mathbf{r}-\mathbf{r}_0)$ is the second order Green's function tensor, $\mathbf{T}(\mathbf{r}-\mathbf{r}_0)$ is the third order tensor defining the stress field due to the Green's function tensor and $\mathbf{n}(\mathbf{r})$ is the normal vector of the surface pointing into the fluid. Here, PV represents the Cauchy principal value of the integral. The Green's function tensor for the unsteady Stokes equations is

$$\mathbf{G}(\mathbf{r}-\mathbf{r}_0) = \frac{A(\bar{r})}{|\mathbf{r}-\mathbf{r}_0|}\mathbf{I} + \frac{B(\bar{r})}{|\mathbf{r}-\mathbf{r}_0|^3}(\mathbf{r}-\mathbf{r}_0)(\mathbf{r}-\mathbf{r}_0), \tag{S32}$$

where $\mathbf{I}$ is the identity tensor, $|\mathbf{r}-\mathbf{r}_0|$ is the distance between $\mathbf{r}$ and $\mathbf{r}_0$, $\bar{r} = |\mathbf{r}-\mathbf{r}_0|(1-i)\sqrt{\beta/2}$ is a scaled length, and

$$A(\bar{r}) = 2\exp(-\bar{r})\left(1+\frac{1}{\bar{r}}+\frac{1}{\bar{r}^2}\right) - \frac{2}{\bar{r}^2}, \tag{S33}$$

$$B(\bar{r}) = -2\exp(-\bar{r})\left(1+\frac{3}{\bar{r}}+\frac{3}{\bar{r}^2}\right) + \frac{6}{\bar{r}^2}. \tag{S34}$$

The stress tensor, $\mathbf{T}(\mathbf{r}-\mathbf{r}_0)$, is not required as we show next.

The noninertial reference frame, where the SMR's internal solid walls (boundaries) are stationary, is used so that the second integral in eq S31 is only over S_p. The boundary conditions on the flow are therefore

$$\mathbf{u} = \mathbf{0}, \qquad \mathbf{r}\in S_c \tag{S35}$$

$$\mathbf{u} = (V-1)\hat{\mathbf{z}}, \qquad \mathbf{r}\in S_p \tag{S36}$$

where $\hat{\mathbf{z}}$ is a Cartesian unit vector in the direction of the oscillatory flow. We now consider a (hypothetical) bulk flow of $\mathbf{u}' = \hat{\mathbf{z}}$ which has pressure $p' = i\beta z$ where z is the coordinate in the direction of $\hat{\mathbf{z}}$. Use of this flow field, the boundary integral equation, eq S31, and the definition of the Green's function tensor, eq S32, leads to the identity,

$$\begin{aligned}PV\int_{S_p}\hat{\mathbf{z}}(\mathbf{r})\cdot[\mathbf{T}(\mathbf{r}-\mathbf{r}_0)\cdot\mathbf{n}(\mathbf{r})]\,dS(\mathbf{r}) \\ = -i\beta\int_{S_p} z\mathbf{n}(\mathbf{r})\cdot\mathbf{G}(\mathbf{r}-\mathbf{r}_0)\,dS(\mathbf{r}) - 4\pi\hat{\mathbf{z}}.\end{aligned} \tag{S37}$$

Substituting eq S37 into eq S31 gives

$$\mathbf{u}(\mathbf{r}_0) = -\frac{1}{8\pi}\int_S \mathbf{F}(\mathbf{r})\cdot\mathbf{G}(\mathbf{r}-\mathbf{r}_0)\,dS(\mathbf{r})\,, \tag{S38}$$

where $\mathbf{u}$ is specified in eqs S35 and S36 and

$$\mathbf{F}(\mathbf{r}) = \mathbf{f}(\mathbf{r}) + i\beta(V-1)z\mathbf{n}(\mathbf{r})\begin{cases}1, & \mathbf{r}\in S_p\\ 0, & \mathbf{r}\in S_c\end{cases}. \tag{S39}$$

Note that the solution to eq S38 does not include the fictitious force due to the noninertial reference frame which must be added to calculate the true force, i.e. $\mathbf{f}_{\text{true}}(\mathbf{r}) = \mathbf{f}(\mathbf{r}) - i\beta z\mathbf{n}$. The mass discrepancy parameter is then calculated in an analogous procedure to that described in Section S5.

The SMR microfluidic channel length and width are considered to be much larger than its height, which allows a local analysis of the particle motion; the SMR is approximated to be infinitely long relative to its height so that the walls move with constant velocity in the vicinity of the particle. An axisymmetric domain is then centered on the particle with the fluid domain along the SMR length and width being infinite; the maximal value of the radial coordinate is increased so that the calculated mass discrepancy parameter is insensitive to this value. An example of

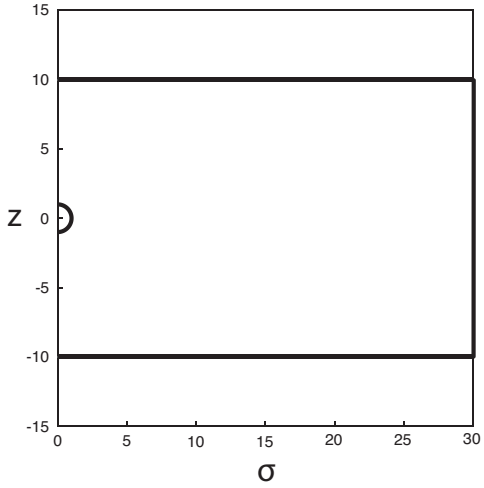

Figure S10. Contour used in axisymmetric boundary integral numerical calculation. Example of the contour used in the boundary integral calculation, in cylindrical polar coordinates; σ and z are the radial and axial coordinates, respectively. The upper and lower horizontal lines correspond to the walls of the SMR's microfluidic channel whereas the semi-circle is the sphere—placed at the center of the microfluidic channel here. The radial extent of this domain is increased so that it does not affect the resulting mass discrepancy parameter.

the axisymmetric fluid domain is given in Figure S10. Equation S38 is transformed into (cylindrical) axisymmetric coordinates, giving

$$\mathbf{u}(\mathbf{r}_0) = -\frac{1}{8\pi}\int_C \mathbf{F}(\mathbf{r})\cdot\mathbf{M}(\mathbf{r}-\mathbf{r}_0)\,dC(\mathbf{r})\,, \tag{S40}$$

where $C = C_p \cup C_c$ is the contour of the particle and the SMR's microfluidic channel, respectively; see Figure S10. The axisymmetric Green's function tensor, $\mathbf{M}$, now represents a ring of point forces and is defined by

$$\mathbf{M} = \sigma\int_0^{2\pi}\{(G_{xx}\cos\phi + G_{xy}\sin\phi)\,\hat{\boldsymbol{\sigma}}\hat{\boldsymbol{\sigma}} + (G_{xz}\cos\phi + G_{yz}\sin\phi)\,\hat{\boldsymbol{\sigma}}\hat{\mathbf{z}} + G_{xz}\hat{\mathbf{z}}\hat{\boldsymbol{\sigma}} + G_{zz}\hat{\mathbf{z}}\hat{\mathbf{z}}\}\,\mathrm{d}\phi, \tag{S41}$$

where ϕ is the azimuthal coordinate normal to the contour, C (which lies in the σ-z plane; see Figure S10) and $\hat{\boldsymbol{\sigma}}$ is the unit vector in the radial σ-direction. G_{xx}, G_{xy} etc. are elements of the Green's function tensor expressed in a Cartesian basis (with coordinates x, y, z); see ref 10 for further details on the implementation of axisymmetric boundary integral methods.

Equation S40 is solved by discretizing the contour, C, into N elements where $\mathbf{F}(\mathbf{r})$ is chosen to be constant on each element; in addition, the ϕ-integration in eq S41 is performed by discretizing its domain into M elements. For the nonsingular elements (i.e., when $\mathbf{r}_0$ is on a different element to $\mathbf{r}$) a 20-point Gaussian-Legendre quadrature scheme is used on both the contour and the ϕ-integration. For the singular elements, the singularity is logarithmic in nature and so a quadrature for logarithmic singularities as described in ref 10 is used. The number of elements required for convergence varies depending on proximity of the particle to the wall and the oscillatory Reynolds number. In general, the larger the oscillatory Reynolds number and closer the particle is to the wall, the greater the number of elements required. For the largest oscillatory Reynolds numbers used throughout this study, if the particle is more than one radius away from any wall then 128 elements (40 on the particle and 88 on the walls) gives convergence in the mass discrepancy parameter, α, of greater than 99.9%. When the particle is in the vicinity of one of the walls, additional elements are included in the lubrication region until convergence of 99.9% is achieved (up to 256 elements are needed which depends on both the channel height and the oscillatory Reynolds number, β).

The mass discrepancy parameter, α, is calculated from the force on the surface of the SMR's microfluidic channel for a particle located at a specific position. Performing these calculations at the oscillatory Reynolds number, β, for each excited mode of the SMR gives the required result for the mass discrepancy parameter, α, for a no-slip particle (in the absence of frequency noise).

Numerical discretization in the boundary element method is systematically refined as discussed above to achieve a convergence of 99.9% in the mass discrepancy parameter; this convergence with increasing discretization is observed to obey a geometric progression. Hence, the discretization error in the evaluated slip length is reduced through the use of Shank's transformation.[11] The difference between the numerical results from Shank's transformation and the finest discretization used in the boundary element method are included in the errors bars of Figures S5 and S4.

S12. EXPERIMENTALLY REALIZABLE MEASUREMENTS

This section lists a series of ready-for-use particle/fluid/SMR systems that provide the basis for future measurements of slip. They use existing and readily available materials and devices. See Table S4 and its caption for details.

Table S4. Experimentally realizable slip measurements. SMRs: Device 1 used in present study; Device 2 has larger channel height of 8 μm ("8×8" device in ref 12). Nanoparticles: Available from Sigma-Aldrich, except large aluminum oxide nanoparticles from MSE Supplies. Surface properties: Gold nanoparticles in citrate buffer, phosphate buffer and thiol coatings. Varying electrolyte concentration allows effect of surface charge on slip length to be studied; see recent molecular dynamics study.[13] Lower limit of particle radius specified by sufficient signal-to-noise; upper limit to minimize effect of SMR bounding walls. All systems use multiple SMR modes with Reynolds numbers 0.1–100, where measurements are most sensitive to slip.

Nanoparticle	Liquid	Radii range (nm)	
		Device 1	Device 2
Gold	Water[(a)]	115-160	150-500
Gold	Water + electrolytes[(b)]	115-160	150-500
Gold	Acetone[(c)]	115-160	150-500
Gold	N-decane[(d)]	115-160	150-500
Gold	Ethanol[(e)]	115-160	150-500
Silver	Liquids (a)–(e)	145-160	200-500
Aluminum oxide	Liquids (a)–(e)	None	300-500
Silica	Liquids (a)–(e)	None	300-500
Gold	Glycerol	None	150-500
Silver	Glycerol	None	200-500

REFERENCES

(1) Olcum, S.; Cermak, N.; Wasserman, S. C.; Manalis, S. R. High-speed multiple-mode mass-sensing resolves dynamic nanoscale mass distributions. *Nat. Commun.* **2015**, 6, 1–8.

(2) Olcum, S.; Cermak, N.; Wasserman, S. C.; Christine, K. S.; Atsumi, H.; Payer, K. R.; Shen, W.; Lee, J.; Belcher, A. M.; Bhatia, S. N.; Manalis, S. R. Weighing nanoparticles in solution at the attogram scale. *Proc. Natl. Acad. Sci. U. S. A.* **2014**, 111, 1310–1315.

(3) Godin, M.; Delgado, F. F.; Son, S.; Grover, W. H.; Bryan, A. K.; Tzur, A.; Jorgensen, P.; Payer, K.; Grossman, A. D.; Kirschner, M. W.; Manalis, S. R. Using buoyant mass to measure the growth of single cells. *Nat. Methods* **2010**, 7, 387–390.

(4) Lee, J.; Shen, W.; Payer, K.; Burg, T. P.; Manalis, S. R. Toward attogram mass measurements in solution with suspended nanochannel resonators. *Nano Lett.*, **2010**, 10, 2537–2542.

(5) Park, J. W.; Shumaker-Parry, J. S. Structural study of citrate layers on gold nanoparticles: Role of intermolecular interactions in stabilizing nanoparticles. *J. Am. Chem. Soc.*, **2014**, 136, 1907–1921.

(6) Yan,H.; Zhang, W. M.; Jiang, H. M.; Hu, K. M.; Hong, F. J.; Peng, Z. K.; Meng, G. A measurement criterion for accurate mass detection using vibrating suspended microchannel resonators. *J. Sound Vib.*, **2017**, 403, 1–20.

(7) Kamrin, K.; Bazant, M. Z.; Stone, H. A. Effective slip boundary conditions for arbitrary periodic surfaces: The surface mobility tensor. *J. Fluid Mech.*, **2010**, 658, 409–437.

(8) Zhang, W.; Stone, H. A. Oscillatory motions of circular disks and nearly spherical particles in viscous flows. *J. Fluid Mech.*, **1998**, 367, 329–358.

(9) Sader, J. E.; Hughes, B. D.; Sanelli, J. A.; Bieske, E. J. Effect of multiplicative noise on least-squares parameter estimation with applications to the atomic force microscope. *Rev. Sci. Instrum.*, **2012**, 83, 5.

(10) Pozrikidis, C. *A Practical Guide to Boundary Element Methods with the Software Library BEMLIB*; CRC Press: Boca Raton, 2002.

(11) Hinch, E. J. *Perturbation Methods*; Cambridge University Press: Cambrdige, UK, 1991.

(12) Katsikis, G.; Collis, J. F.; Knudsen, S. M.; Agache, V.; Sader, J. E.; Manalis, S. R. Inertial and viscous flywheel sensing of nanoparticles. arXiv:2011.06184 **2020**.

(13) Xie, Y.; Fu, L.; Niehaus, T.; Joly, L. Liquid-Solid Slip on Charged Walls: The Dramatic Impact of Charge Distribution. *Phys. Rev. Lett.*, **2020**, 125, 014501.